Ultramicroscopy 110 (2010) 891–898

Contents lists available at ScienceDirect

Ultramicroscopy

journal homepage: www.elsevier.com/locate/ultramic

Aberration measurement using the Ronchigram contrast transfer function

A.R. Lupini [a,*], P. Wang [b], P.D. Nellist [b], A.I. Kirkland [b], S.J. Pennycook [a]

[a] Materials Science and Technology Division, Oak Ridge National Laboratory, Oak Ridge, TN 37831, USA
[b] Department of Materials, University of Oxford, Parks Road, Oxford OX1 3PH, UK

ARTICLE INFO

Article history:
Received 24 October 2009
Received in revised form
28 March 2010
Accepted 13 April 2010

Keywords:
Aberration measurement
Aberration correction
Ronchigram
Inline hologram
Contrast transfer function
STEM
TEM

ABSTRACT

The bright field contrast transfer function is one of the most useful concepts in conventional transmission electron microscopy. However, the electron Ronchigram contrast transfer function, as derived by Cowley, is inherently more complicated since it is not isoplanatic. Here, we derive a local contrast transfer function for small patches in a Ronchigram and demonstrate its utility for the direct measurement of aberrations from single Ronchigrams of an amorphous film. We describe the measurement of aberrations from both simulated and experimental images and elucidate the effects due to higher-order aberrations, separating those arising from the pre- and post-sample optics, and partial coherence.

Published by Elsevier B.V.

1. Introduction

Following recent advances in aberration-corrected scanning transmission electron microscopy (STEM) [1–5], there is now renewed interest in methods for the measurement of aberrations in this mode. Many of the currently reported aberration measurement methods require several images [6–12] and are therefore relatively slow and are subjected to specimen drift that can corrupt the data. The electron Ronchigram already provides a well-established method [8] for the measurement of aberrations using several images. Developments in aberration measurement for STEM using the Ronchigram include methods that analyze a form of Ronchigram taken while changing focus [13], using autocorrelations from amorphous samples [14], or using Fourier transforms of crystalline samples [15]. However, the latter two methods (for unknown samples) rely on an accurate prior calibration of the defocus to produce absolute aberration measurements. In this paper, we describe a method for aberration measurement from a single Ronchigram of an amorphous material, using a set of Fourier transforms. Our analysis produces absolute values of the aberration coefficients, including defocus and additionally provides useful information on the degree of coherence. Future improvements in the accuracy of this method are also discussed.

2. The contrast transfer function for a small patch in a Ronchigram

An inline hologram can be formed by using an objective lens to focus a beam of electrons to a small probe at or near to the plane of a sample [16]. The electrons propagate through the sample and the resulting shadow-image in the far-field is commonly known as the Ronchigram [17–19]. Here, we initially assume that the objective aperture is uniformly and coherently illuminated by a monochromatic beam of electrons. We will subsequently show that these assumptions are not strict requirements for the method described, as both temporal and spatial incoherence can be included within our formulation. For a thin sample, we further assume that the transmitted wavefunction is given by the real-space product of the sample function Ψ and the probe P, which is itself given by the (inverse) Fourier transform of the wavefield at the objective aperture.

Under these assumptions the intensity I of the Ronchigram recorded at the detector plane as a function of the scattered wavevector $\mathbf{K}_f$ and probe position $\mathbf{R}_0$ is given by

$$I(\mathbf{K}_f,\mathbf{R}_0)=\iint \Psi(\mathbf{K}_f-\mathbf{K}_i)\cdot\overline{\Psi(\mathbf{K}_f-\mathbf{K}_j)}\cdot e^{-2\pi\lambda^{-1}i[\chi(\mathbf{K}_i)-\chi(\mathbf{K}_j)]}\cdot e^{2\pi\lambda^{-1}i(\mathbf{K}_i-\mathbf{K}_j)\cdot\mathbf{R}_0}d\mathbf{K}_i d\mathbf{K}_j, \quad (1)$$

where λ is the electron wavelength, $\mathbf{K}_i$ and $\mathbf{K}_j$ are the incident wavevectors, $\overline{\Psi}$ is the complex conjugate of Ψ and χ is the aberration phase function described in Appendix A and in Ref. [8].

In the Ronchigram configuration shown in Fig. 1, rays traveling at large angles to each other pass through different parts of the sample. For an amorphous sample, in contrast to a crystalline

* Corresponding author.
E-mail address: arl1000@ornl.gov (A.R. Lupini).

0304-3991/$ - see front matter Published by Elsevier B.V.
doi:10.1016/j.ultramic.2010.04.006

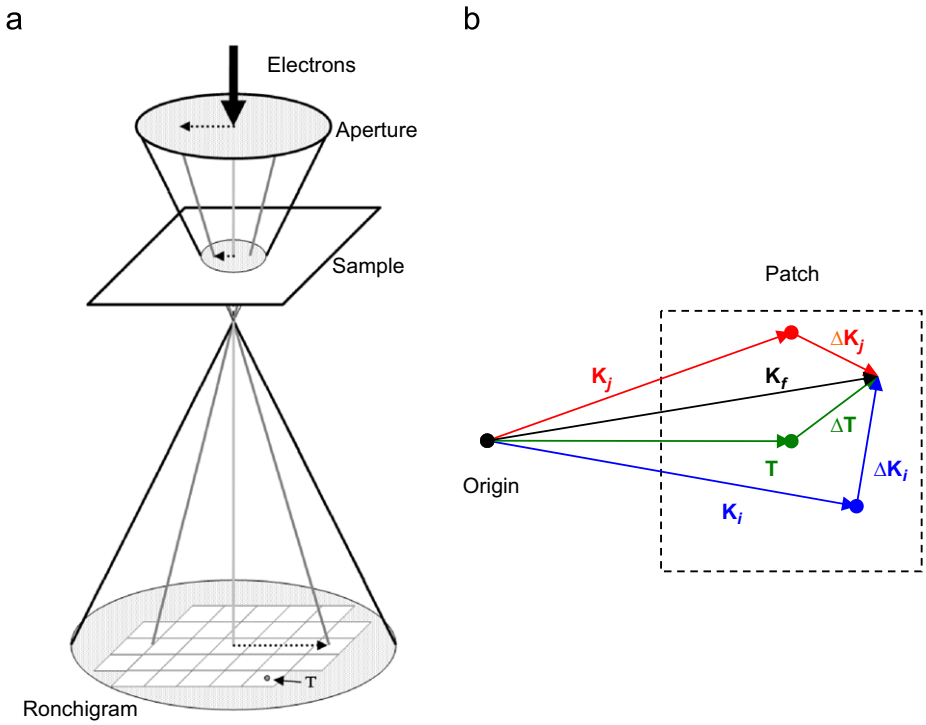

Fig. 1. (a) Schematic formation of an electron Ronchigram or 'shadow image' and the division of the Ronchigram into small patches. Each patch corresponds to a different scattering angle (i.e. patch **T**). (b) Schematic diagram showing scattering from incident angles $\mathbf{K}_i$ and $\mathbf{K}_j$ into a particular final angle $\mathbf{K}_f$ that is within a patch centered at **T**. Although none of these angles are necessarily small, with an amorphous specimen the scattering decreases with angle, so that the only significant contributions (denoted Δ) involve small angle scattering.

material, there is no fixed phase relationship for the scattering from spatially separate atoms. Thus, for an amorphous specimen coherent interference effects at large angles cancel, leaving an intensity dominated by small-angle scattering. The differences between the incident and scattered wavevectors can therefore be defined as $\Delta\mathbf{K}_i=\mathbf{K}_f-\mathbf{K}_i$ and $\Delta\mathbf{K}_j=\mathbf{K}_f-\mathbf{K}_j$, respectively, where $\Delta\mathbf{K}_i$ and $\Delta\mathbf{K}_j$ are small. Substituting for $\mathbf{K}_i$ and $\mathbf{K}_j$ in Eq. (1) and setting $\mathbf{R}_0=0$ (considering just one probe position to simplify the notation) gives

$$I(\mathbf{K}_f)=\iint \Psi(\Delta\mathbf{K}_i)\cdot\overline{\Psi(\Delta\mathbf{K}_j)}\cdot e^{-2\pi\lambda^{-1}i[\chi(\mathbf{K}_f-\Delta\mathbf{K}_i)-\chi(\mathbf{K}_f-\Delta\mathbf{K}_j)]}d\Delta\mathbf{K}_i\,d\Delta\mathbf{K}_j. \quad (2)$$

However, the Ronchigram is non-isoplanatic [20] across its recorded field of view, which complicates the derivation of a suitable contrast transfer function (CTF). One approach to overcoming this difficulty is to divide the Ronchigram into an array of small patches, *e.g.* an $n\times n$ array as shown in Fig. 1(a), such that each small patch can be considered as isoplanatic. Fig. 1(b) schematically illustrates the relation between the wavevectors for a vector $\mathbf{K}_f$ at a small distance $\Delta\mathbf{T}$ from the center of such a patch at a particular angle **T**.

It is convenient to define a new function $\chi_{\mathbf{T}}(\Delta\mathbf{T})$ as the difference between the aberration function evaluated at two slightly different angles $\mathbf{T}+\Delta\mathbf{T}$ and **T**, which can be Taylor series expanded as (Appendix B)

$$\begin{aligned}\chi_{\mathbf{T}}(\Delta\mathbf{T}) &:= \chi(\mathbf{T}+\Delta\mathbf{T})-\chi(\mathbf{T})=\Delta\mathbf{T}\cdot\nabla\chi(\mathbf{T})+\frac{1}{2}\cdot\Delta\mathbf{T}\cdot\underline{\mathbf{H}}_{\mathbf{T}}\cdot\Delta\mathbf{T}+O(\Delta\mathbf{T}^3)\\ &:= \Delta\mathbf{T}\cdot(C^{\mathbf{T}}_{01a},C^{\mathbf{T}}_{01b})+\frac{1}{2}\Delta\mathbf{T}\cdot\begin{pmatrix}C^{\mathbf{T}}_1+C^{\mathbf{T}}_{12a} & C^{\mathbf{T}}_{12b}\\ C^{\mathbf{T}}_{12b} & C^{\mathbf{T}}_1-C^{\mathbf{T}}_{12a}\end{pmatrix}\cdot\Delta\mathbf{T}+O(\Delta\mathbf{T}^3),\end{aligned} \quad (3)$$

where $\underline{\mathbf{H}}_{\mathbf{T}}$ is the Hessian matrix of second derivatives of the aberration function χ at a tilt angle **T**. We note that $\chi_{\mathbf{T}}(\Delta\mathbf{T})$ has the same form as $\chi(\mathbf{K})$ although the values of the coefficients are changed. Here, we have used superscripts to indicate apparent aberration coefficients $C^{\mathbf{T}}$ evaluated at a tilt angle **T** since they differ from the axial values. In this formulation, there is a direct correspondence for tilted detection angles in STEM to the changes in measured aberrations in the TEM geometry under tilted incident illumination [9–12,21]. As an example, the constant term in the apparent astigmatism $C^{\mathbf{T}}_{12a}$ is the axial value of astigmatism in the *a*-direction C_{12a} but there are additional polynomial contributions from higher-order aberrations that cause the apparent astigmatism to vary with angle from the optical axis.

We now consider a beam at a particular angle, $\mathbf{K}_f$ arriving at a patch centered at **T** in the Ronchigram. The intensity within this small patch at an angle **T** can be written in the following approximate form, following Eq. (2) as

$$I(\mathbf{T},\Delta\mathbf{T})=\iint \Psi(\Delta\mathbf{K}_i)\cdot\overline{\Psi(\Delta\mathbf{K}_j)}\cdot e^{-2\pi\lambda^{-1}i[\chi(\mathbf{T}+\Delta\mathbf{T}-\Delta\mathbf{K}_i)-\chi(\mathbf{T}+\Delta\mathbf{T}-\Delta\mathbf{K}_j)]}d\Delta\mathbf{K}_i d\Delta\mathbf{K}_j. \quad (4)$$

Clearly, there are some limitations to this approximation that may not be mathematically rigorous at discontinuities or at loci of infinite magnification, and the criteria defining a "small" patch will depend on the aberrations to be measured. However, the utility of this equation is that as all the difference terms Δ are small we can Taylor expand the exponential and neglect higher-order terms in $\chi_{\mathbf{T}}$ (Appendix B) giving

$$\begin{aligned}&\chi(\mathbf{T}+\Delta\mathbf{T}-\Delta\mathbf{K}_i)-\chi(\mathbf{T}+\Delta\mathbf{T}-\Delta\mathbf{K}_j)\\ &\quad\approx\chi(\mathbf{T}-\Delta\mathbf{K}_i)-\chi(\mathbf{T}-\Delta\mathbf{K}_j)-\Delta\mathbf{T}\cdot\underline{\mathbf{H}}_{\mathbf{T}}\cdot(\Delta\mathbf{K}_i-\Delta\mathbf{K}_j).\end{aligned} \quad (5)$$

Using this approximation the Fourier transform of Eq. (4) for a small patch centered at **T** with respect to $\Delta\mathbf{T}$ (Appendix C) will contain a Dirac delta function

$$\delta(\underline{\mathbf{H}}_{\mathbf{T}}\cdot\Delta\mathbf{K}_j-\underline{\mathbf{H}}_{\mathbf{T}}\cdot\Delta\mathbf{K}_i-\boldsymbol{\tau}), \quad (6)$$

where $\boldsymbol{\tau}$ is the conjugate variable to $\Delta\mathbf{T}$. One difficulty in developing this approach is that the mathematical notation quickly becomes unwieldy, even for the simpler 1-dimensional case (e.g. [18]). Therefore, a useful simplification is to rewrite this delta function as

$$\delta(\Delta\mathbf{K}_j - \Delta\mathbf{K}_i - \underline{\mathbf{H}}_{\mathbf{T}}^{-1}\cdot\boldsymbol{\tau}), \tag{7}$$

where we have used $\underline{\mathbf{H}}_{\mathbf{T}}^{-1}$ as the inverse of the matrix of second derivatives evaluated for a tilt $\mathbf{T}$, which is only applicable where the matrix $\underline{\mathbf{H}}_{\mathbf{T}}$ is invertible.

Thus

$$\begin{aligned}\tilde{I}(\mathbf{T},\boldsymbol{\tau}) &= FT(I(\mathbf{T},\Delta\mathbf{T})) \\ &= \int \Psi(\Delta\mathbf{K}_i)\cdot\overline{\Psi(\Delta\mathbf{K}_i+\underline{\mathbf{H}}_{\mathbf{T}}^{-1}\cdot\boldsymbol{\tau})} \\ &\quad\cdot e^{-2\pi i\lambda^{-1}\cdot[\chi(\mathbf{T}-\Delta\mathbf{K}_i)-\chi(\mathbf{T}-\Delta\mathbf{K}_i-\underline{\mathbf{H}}_{\mathbf{T}}^{-1}\cdot\boldsymbol{\tau})]}d\Delta\mathbf{K}_i.\end{aligned} \tag{8}$$

The specimen is now approximated as a weak-phase object

$$\Psi(\mathbf{K}) \approx \delta(\mathbf{K}) - i\sigma\tilde{V}(\mathbf{K}) \tag{9}$$

in reciprocal space, where $\delta(\mathbf{K})$ is the Dirac delta function and $\sigma\tilde{V}(\mathbf{K})$ is the Fourier transform of the projected potential of the specimen multiplied by an interaction constant. The Fourier transform of a small patch in the Ronchigram for a weak-phase object can thus be conveniently expressed (Appendix D) by retaining only the linear terms in $\sigma\tilde{V}(\mathbf{K})$ from Eq. (8) as

$$\tilde{I}(\mathbf{T},\boldsymbol{\tau}) \approx 2\sigma\tilde{V}\left(-\underline{\mathbf{H}}_{\mathbf{T}}^{-1}\cdot\boldsymbol{\tau}\right)\sin\left[2\pi\lambda^{-1}\chi_{\mathbf{T}}^{even}\left(-\underline{\mathbf{H}}_{\mathbf{T}}^{-1}\cdot\boldsymbol{\tau}\right)\right]\cdot e^{-2\pi i\lambda^{-1}\chi_{\mathbf{T}}^{odd}\left(-\underline{\mathbf{H}}_{\mathbf{T}}^{-1}\cdot\boldsymbol{\tau}\right)}, \tag{10}$$

where $\chi_{\mathbf{T}}^{even}$ and $\chi_{\mathbf{T}}^{odd}$ denote the even and odd parts of the aberration function $\chi_{\mathbf{T}}$, respectively.

In order to compare this new result to a more familiar one, we can derive the CTF for tilted bright field (BF) imaging by Fourier transforming Eq. (1) from the probe coordinate $\mathbf{R}_0$ to spatial frequency $\boldsymbol{\rho}$ (Appendix E), using the same approximations, to give

$$I(\mathbf{T},\boldsymbol{\rho}) = 2\sigma V(\boldsymbol{\rho})\sin[2\pi\lambda^{-1}\chi_{\mathbf{T}}^{even}(\boldsymbol{\rho})]e^{-2\pi\lambda^{-1}\chi_{\mathbf{T}}^{odd}(\boldsymbol{\rho})}. \tag{11}$$

We note that Eq. (11) simplifies to the more usual form for BF imaging for an on-axis detector (when $\mathbf{T}=0$). However, Eq. (11) also applies to off-axial imaging and recalling that the aberration function $\chi_{\mathbf{T}}$ is a power series, it is apparent that tilted BF images will be similar to on-axis BF images, but with different (tilted) aberration coefficients. Thus, it is shown that recording a BF STEM image with a tilted detector is a direct parallel to recording a BF TEM image with tilted illumination [6,9–12,21], entirely in accord with the principle of reciprocity [22–23].

Comparison of Eqs. (10) and (11) demonstrates that both the Fourier transform of a tilted BF STEM image and the Fourier transform of a patch of the Ronchigram show the familiar series of light and dark rings, which resemble the Thon rings of the BF TEM CTF [9–12,21] and whose positions depend on the even part of the wave aberration function. In the case of the Ronchigram, however, the variable $\boldsymbol{\tau}$ is magnified by a non-isotropic matrix which varies with tilt angle that also needs to be considered in order to interpret the ring positions.

We now make use of the following approximation when first-order effective aberrations dominate $\chi_{\mathbf{T}}^{even}$ (see Appendix D):

$$\chi_{\mathbf{T}}^{even}(\boldsymbol{\tau}) \approx \frac{1}{2}\boldsymbol{\tau}\underline{\mathbf{H}}_{\mathbf{T}}\boldsymbol{\tau} + \cdots, \tag{12}$$

which allows us to simplify the expression for the Ronchigram patch CTF as

$$\mathrm{CTF}_{Ronchi}(\mathbf{T},\boldsymbol{\tau}) \approx \sin\left(\pi\lambda^{-1}\boldsymbol{\tau}\underline{\mathbf{H}}_{\mathbf{T}}^{-1}\boldsymbol{\tau}\right). \tag{13}$$

Applying the same approximation (that $\chi_{\mathbf{T}}^{even}$ is dominated by first-order terms) to the BF CTF gives the CTF of a BF image with a tilted detector as

$$\mathrm{CTF}_{BF}(\mathbf{T},\boldsymbol{\rho}) \approx \sin(\pi\lambda^{-1}\boldsymbol{\rho}\underline{\mathbf{H}}_{\mathbf{T}}\boldsymbol{\rho}). \tag{14}$$

This illustrates the familiar result that the Fourier transform of a BF image has a series of light and dark rings, the radii of which can be used to determine the effective defocus and astigmatism (which provide the elements of the matrix $\underline{\mathbf{H}}_{\mathbf{T}}$). Therefore, repeating these measurements on several different BF images recorded at different tilts (an effective Zemlin tableau [12]) enables the entire aberration function to be fitted, as has been extensively used for aberration measurement in the TEM geometry [9–12,21].

Comparison of Eqs. (13) and (14) shows that the only significant difference is the matrix inversion of $\underline{\mathbf{H}}_{\mathbf{T}}$. This result is important as it reveals that the effective aberrations from a small patch in a Ronchigram vary in a similar, albeit reciprocal, way to the effective aberrations in a tilted BF image [9–12,21]. Thus, our method for aberration measurement is relatively simple: we extract a series of small patches from the Ronchigram; then Fourier transform and analyze each patch to give an array of estimates of the second derivatives to which we fit an aberration function. Moreover, our approach to aberration measurement in STEM is a direct analog to aberration measurement from a Zemlin tableau in TEM, except that instead of requiring many images, we simply cut many patches from a single Ronchigram.

An important difference is that for tilted BF images the tilt $\mathbf{T}$ and spatial frequency $\boldsymbol{\rho}$ are largely independent, whereas in an analysis of the Ronchigram the variable $\boldsymbol{\tau}$ is the conjugate of a tilt angle. Finally, we emphasize that our assumption that the aberration function is dominated by first order aberration coefficients may lead this algorithm to an incorrect answer when this is not the case, which in turn suggests that defocus should be chosen appropriately to allow accurate higher-order measurements. Accordingly, whilst we use Eq. (13) in the experimental section of the present work we note that the more accurate Eq. (10) might be explored in the future.

3. The effects of limited coherence

The theory detailed in the previous section describes the coherent contrast transfer function for small patches extracted from an electron Ronchigram and provides a route for aberration measurement. However, it is also possible to use the same mathematical framework to analyze the effects of limited coherence. The spatial coherence damping envelope E_s, caused by the finite size of the effective electron source [24–29] is given by integration over a Gaussian source with $1/e$ width w at the sample. Applying the same delta-function approximation gives the expression (Appendix F):

$$E_s(\mathbf{T},\boldsymbol{\tau}) \propto e^{-(w\pi\lambda^{-1}\underline{\mathbf{H}}_{\mathbf{T}}^{-1}\boldsymbol{\tau})^2}. \tag{15}$$

This equation provides two routes for further analysis. Firstly, if the effective source size can be independently estimated, it is possible to fit the damping envelopes and determine the local second derivatives of the aberration function from those as an alternative to using the CTF rings. We note that this alternative would be related to the method described by Sawada et al. [14], who utilize the autocorrelation function (ACF) and fit a Gaussian, because the width of each ACF central maximum in that work depends upon the damping envelope. Secondly, determination of the aberrations as already described enables Eq. (15) to measure the effective source size. Using this latter approach, the source size determined from simulated Ronchigrams is expected to match the effective size. However, for the experimental data shown in Figs. 4–6 the effective source width measured at the

sample plane was typically ca. 0.1 nm. This value probably overestimates the true size, as our analysis ignores other experimental effects that contribute to contrast damping, such as noise, sampling limitations, patch size, chromatic aberration and details of the sample scattering function.

We next consider the effect of damping due to chromatic aberration. The temporal coherence damping envelope E_Δ is given by integration over a chromatic focus spread Δ [26,28,30] as approximately (Appendix G):

$$E_\Delta^{\pm}(\mathbf{T},\boldsymbol{\tau}) \propto e^{-\left(\left(\pm 2\mathbf{T}\cdot\underline{\mathbf{H}}_{\mathbf{T}}^{-1}\cdot\boldsymbol{\tau}+\left(\underline{\mathbf{H}}_{\mathbf{T}}^{-1}\cdot\boldsymbol{\tau}\right)^2\right)\pi\Delta/(2\lambda)\right)^2}. \tag{16}$$

In Eq. (16) we have used $\pm$ as a nomenclature to indicate that there are different damping envelopes operating on each of the two linear terms that contribute to a particular spatial frequency (as in Ref. [30] for tilted illumination). The even (symmetrical) damping term leads to the CTF given earlier and so we now consider that term in more detail:

$$E_\Delta(\mathbf{T},\boldsymbol{\tau}) \propto \exp\left(-\left(\frac{\pi\Delta}{2\lambda}\right)^2\left(4\left(\mathbf{T}\cdot\underline{\mathbf{H}}_{\mathbf{T}}^{-1}\cdot\boldsymbol{\tau}\right)^2+\left(\underline{\mathbf{H}}_{\mathbf{T}}^{-1}\cdot\boldsymbol{\tau}\right)^4\right)\right). \tag{17}$$

On the optic axis, at $\mathbf{T}=0$, only the second term of Eq. (17) is non-zero and thus at low angles the approximation that the Ronchigram CTF damping is dominated by the source size [14,27] is valid. However, the first term in Eq. (17) increases with off axial distance, resulting in non-isotropic chromatic damping dominating at higher tilt angles. This transition occurs when $|\mathbf{T}|\Delta \approx w$, but should not be significant for the analysis reported here, where we do not rely completely on a particular form for the damping envelope. Thus, by accurately fitting the damping envelopes for axial patches Eq. (15) can be used to measure the effective source size. For off-axis patches, where the effects of chromatic aberration become significant, it should be possible to simultaneously measure the chromatic focus spread using Eq. (16). In future work, it will also be necessary to include this chromatic term in order to more accurately match the damping envelope for patches at high angles.

Our final observations are that Eq. (17) closely resembles the BF TEM off-axial temporal coherence damping envelope [30] and that the CTF (Eq. (10)) closely resembles the BF TEM formulation [6]. The essential difference is that the derivation reported here for STEM replaces the spatial frequency ($\boldsymbol{\rho}$) in the equivalent BF TEM formulae with a magnified local position that also depends on the tilt angle ($\underline{\mathbf{H}}_{\mathbf{T}}^{-1}\boldsymbol{\tau}$).

4. Experimental

Eq. (13) provides a simple means by which the theory outlined in the previous sections can be tested in order to obtain an approximate measure of defocus. Where all aberrations apart from defocus are negligible the first zero of that equation is given by;

$$C_{10} = S_{1st}^2\lambda \tag{18}$$

with C_{10} the defocus, λ the electron wavelength and S_{1st} the radius of the first zero in the CTF. If the first zero is r pixels away from the center of an n pixel wide Fourier transform of a Ronchigram sampled at c radians per pixel then $S_{1st}=r/(cn)$ with $S=|\boldsymbol{\tau}|/\lambda$. Eq. (18) is useful in this regard as it provides a rapid measurement of defocus from a single Ronchigram that can be used to measure chromatic effects or as part of a comparison with other autotuning methods. Fig. 2(a) shows a simulated Ronchigram where it is apparent that the first zero of the CTF obeys Eq. (18), with $r\approx 25$, $n=512$, $c=7.81e^{-5}$ rad/pixel, $\lambda=2.51$ pm, whilst noting that this agreement is approximate due to the limited number of pixels and a non-zero C_{30}. All simulations reported here use a wave-optical method following Eq. (1) for a thin, random phase object with an arbitrary Gaussian feature size imposed. In future it would be of interest to extend the simulations with the use of the correct atomic scattering functions and realistic amorphous models, which would allow the effects of partial ordering and sample thickness to be explored.

Given that a diffractogram calculated from a real image is centrosymmetric, aberration measurement method reliant on diffractograms requires either prior information or suitably conditioned multiple image datasets to determine the sign of defocus. Prior to C_{30}-correction $C_{30}>0$ could be assumed. It is also possible to use Fresnel effects at the edges of particles or surfaces to decide the defocus sign. To automate this determination, two Ronchigrams separated by a known change in lens current can be used. Subsequently we assume that the sign of the defocus is known.

We have conducted tests to verify the validity of Eq. (18) by comparison with the method described in [15]. In general our new method agrees with these alternatives and the small discrepancies measured were attributed to calibration errors.

4.1. A simple automated method

Implementation of a simple automated fitting of Eq. (13) to experimental data requires that each patch in the Ronchigram is sufficiently small such that the aberrations do not vary significantly over the patch, but large enough that the diffractograms are of reasonable quality. Various methods for extracting effective defocus and astigmatism have been described for BF images [9–12,21]. However, these are difficult to be implemented, where sub-pixel fitting accuracy is required for noisy data. One possible approach is to take the diffractogram of a patch, and remap it such that a pixel at radius r and angle θ is mapped onto an array at position (r^2, θ) in which a row consequently describes an angular wedge in the diffractogram [31]. In this scheme each row can be Fourier transformed to give an effective defocus in the direction θ wherein the average gives the focus and the variation gives the astigmatism. Whilst this method is not optimal it is adequate for initial evaluation. Each patch thus gives a local measure of the second derivatives of the aberrations, and measurements from a series of patches allow the full aberration function to be fitted. To perform this fitting, we have used the form of the aberration function given in [8] to derive analytic expression for the effective defocus and astigmatism at each patch where the order of the fit can be altered by changing the number of terms included. Finally, we combined the analytic expressions and measured values into matrices, such that a simple least-squares fit [32] produces estimates for the aberrations.

To analyze the error in this method, a series of 10 simulated Ronchigrams was calculated at different C_{10} values, in -100 nm steps from -1000 to -1900 nm and analysed using a simple script to automate the fitting of the aberrations to third order. The measured aberrations for a 5×5 array of 256×256 pixel patches from this dataset are summarized in Table 1 in which the focus error ΔC_{10} is defined as the difference between the measured and input values. It is notable that C_{30} is generally underestimated whilst C_{10} is overestimated, which emphasizes the difficulty in distinguishing aberrations of the same rotational symmetry but with different orders. Repeating this simulation using positive C_{10} from 1000 to 1900 nm (data not shown) reduced the error in the measurement of C_{30} but increased the error in measurement of C_{10}.

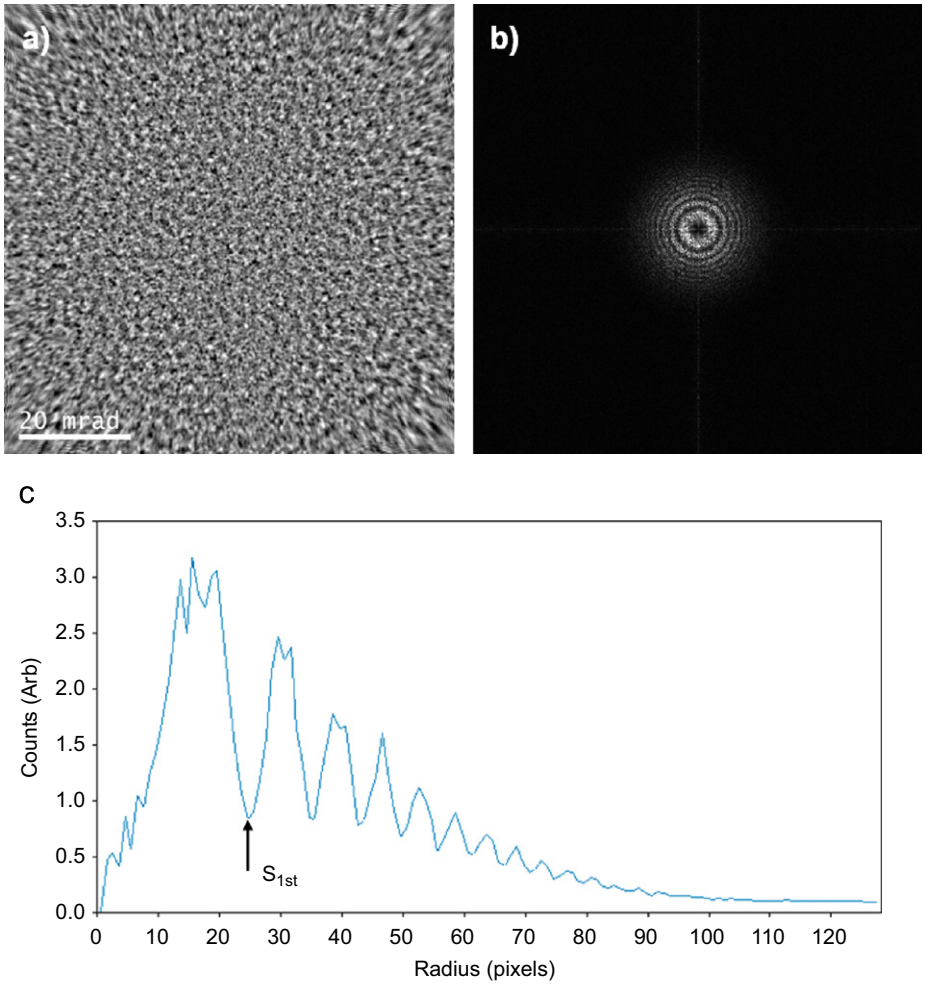

Fig. 2. (a) Simulated Ronchigram for a defocus, $C_{10}=-1000$ nm and spherical aberration, $C_{30}=0.1$ mm and with other aberrations equal to zero at 200 kV. Note how the magnification changes towards the corners of the image. (b) Fourier transform of the 512×512 pixel central patch showing a pattern of light and dark rings. (c) The radial profile of the Fourier transform in (b). The arrow indicates the 'first zero' in the CTF oscillation.

Table 1
Measured aberrations (all/nm) for an 5×5 array of 256×256 pixel patches, spaced by 100 pixels for simulations with $C_{30}=0.1$ mm and with other aberrations set to zero. Averages and standard deviations are given for a 10 frame series from -1000 to -1900 nm defocus.

	ΔC_{10}	C_{12}	C_{23}	C_{21}	C_{30}
Average	3.8	2.3	14.9	23.8	89799
Deviation	5.7	3.6	35.5	37.9	11014
True	0	0	0	0	100000

Table 2
Measured aberrations (all/nm) for an 5×5 array of 256×256 pixel patches, spaced by 100 pixels for a simulation with $C_{12}=50$ nm, $C_{21}=1000$ nm and other aberrations set to zero. Averages and standard deviations are given for a 10 frame series from -1000 to -1900 nm defocus.

	ΔC_{10}	C_{12}	C_{23}	C_{21}	C_{30}
Average	−6.7	49.7	18.1	1002.0	−1355
Deviation	5.3	4.3	57.0	89.4	4620
True	0	50	0	1000	0

To examine the effect of non-round aberrations we have repeated simulations for a series of Ronchigrams calculated for the same focus range with non-zero astigmatism and coma ($C_{12}=50$ nm, $C_{21}=1000$ nm) (Table 2). We conclude that the errors in the first order aberrations are of order a few nm, the errors in the second order aberrations are of order a few tens of nm and the error in the C_{30} is of order a few microns. Most of these errors appear to arise from inaccuracies in fitting the diffractograms. Adding more patches, or repeating the simulations with more pixels, improves the accuracy as expected, but at the expense of increased computational time. By way of illustration, using a script entirely written in the interpreted Gatan DigitalMicrograph scripting language running on a desktop PC, these third-order measurements took of the order of a second per frame. However, in principle, any algorithm that proceeds by dividing a Ronchigram into many small pieces should parallelize and an optimized code in a suitable compiled language might be expected to provide measurements many times per second.

In addition to computational speed, another factor that has to be considered for patch choice is that the aberrations should not vary too much within a 'small' patch. In practice, patch size and detector pixel size provide another limitation to information transfer. The effective aberrations change across larger patches and the pixels must be small enough to record sufficiently fine details. Thus, the criteria for the choice of patch size and position may vary with the magnitude of the aberrations, recorded tilt angles and sample properties. Similarly, although

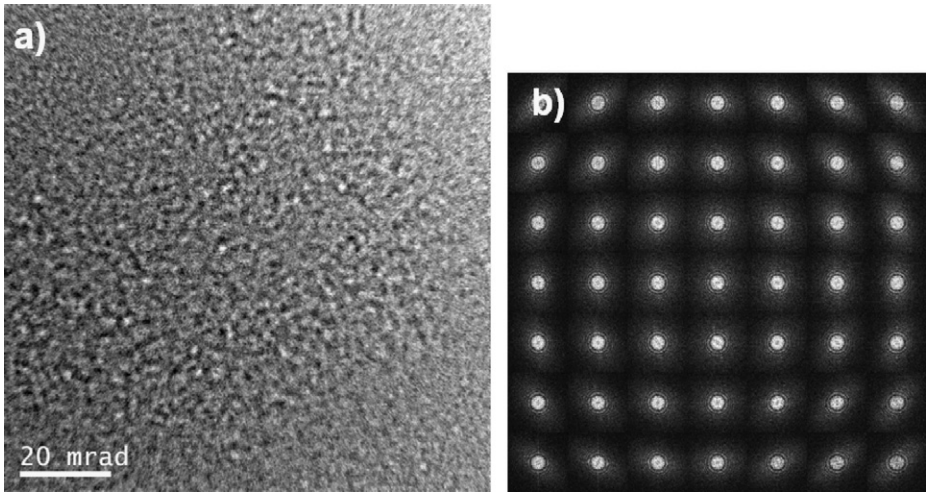

Fig. 3. (a) Experimental electron Ronchigram recorded using the JEOL 2200MCO at Oxford as described in the text. (b) Array of 128 × 128 pixel regions extracted from the Fourier transforms of 256 × 256 pixel patches within the Ronchigram displayed at the positions corresponding to the center of the patches.

the measurement of C_{10} is relatively reliable, the absolute defocus used is important in determining the accuracy of the other terms. Although we have assumed that first order terms are dominant, higher-order terms still need to be measurable. Currently, these choices are left to the user, but our work indicates that an algorithm that predicts an optimal defocus or adaptively varies the patch size could be developed.

Having established that the automated method described works for simulated data, we have subsequently obtained experimental Ronchigrams for further verification. For experimental data we have found that it is important to calibrate the angular scale c accurately. The method used was to form a diffraction pattern by suitable adjustment of the condenser lenses, while keeping all other lenses at the settings used to record the Ronchigram. It is also important to have a thin, amorphous sample that generates clearly recogniseable rings in the Fourier transform. We have tested the algorithm on several different aberration-corrected microscopes (provided by Nion, FEI and JEOL) to date and have found that this method can be implemented on any microscope able to record suitable Ronchigrams.

Fig. 3(a) shows a typical Ronchigram recorded at 200 kV on a JEOL 2200MCO for which the patch Fourier transforms (Fig. 3(b)) show rings suitable for processing. Analysis of this data reveals two noteworthy phenomena. Firstly, the nominal focus values reported by the microscope are often approximate and hence require independent calibration. Secondly, an improbably large two-fold astigmatism value was occasionally measured that changed approximately proportionally to defocus. An obvious source of this error is cross-talk between aberrations of different orders with the same symmetry. However, this explanation would give rise to an error that does not increase strongly with defocus and which should decrease if more patches are used in the analysis (counter to the experimental observations).

Extensive simulations suggest that this error in the measured astigmatism arises from post-sample imaging distortions, which were not included in our previous description. Therefore, we have modeled these (to first order) as a simple difference in vertical and horizontal magnification with respect to the detector coordinate frame, and have been able to reproduce the same effect. This is equivalent to using a mrad/pixel calibration c that varies in different directions. Although this error is a potential experimental problem, in principle, it means that it is possible to measure the post-sample aberrations by analyzing the variation in the measured aberrations with defocus. As an illustrative example, at large defocus values, where the astigmatism from the objective pre-field makes a relatively small contribution to the matrix $\underline{\mathbf{H}}_{\mathbf{T}}$, the measured astigmatism is dominated by the post-sample distortion.

In addition, the astigmatism error introduced is larger in this method, which depends on the square of the calibration c than in a probe-shifting algorithm [8], which has a linear dependence on c. Thus, comparing measured aberrations from different methods should provide another route by which the pre- and post-sample aberrations can be separated. However in the present work, we have used post-specimen stigmators to minimize this effect in the experimental data and have not quantified these post-sample aberrations.

4.2. Higher-order aberrations and an iterative method

While the above method worked well for the simulations, it was found to be inadequate when the residual higher-order aberrations were significant. Since the notation used here was deliberately chosen to apply to arbitrary orders, we included all axial geometrical aberrations up to fifth-order by deriving the second derivatives of each aberration and including these in the matrix $\underline{\mathbf{H}}_{\mathbf{T}}$. The next problem is that it is very hard to fit accurate values to the inaccurately measured diffractograms. To improve our fitting of the experimental data we have developed an iterative algorithm, similar to established methods for TEM diffractogram fitting [9–12,21]. The method used is summarized as follows:

(1) A first pass of the measurement routine, as described in the previous section, was performed to produce a series of measurements of the effective defocus and astigmatism for each patch, to which an initial aberration function was fitted.
(2) A second pass was subsequently carried out using the initially fitted aberrations to estimate the effective defocus and astigmatism for each patch. Using these values CTFs were simulated (including a damping envelope) and the chi-squared difference between each simulated CTF and the corresponding experimental CTF was evaluated. These differences were minimized by varying the values used for each simulated CTF *via* a simple stepping algorithm loosely based on the 'simplex' method [32], similar to methods previously used for TEM diffractogram fitting [9–12,21]. This process produced refined measurements of the effective defocus and

astigmatism, to which a 'refined' aberration function was fitted.

(3) The second pass was repeated as necessary and the convergence was monitored. The convergence of this process to a 'final' value thus provides an indication as to the reliability of the measurement.

The iterative method described here is slow, but serves as a proof of concept. In order to match the CTF it was necessary to include a damping envelope to avoid the algorithm trying to match high-frequency noise. For simplicity, we have assumed that the damping was dominated by spatial coherence (source size) and hence did not include effects due to temporal coherence.

Table 3
Repeats of the measurement in Table 1, for a simulation with C_{30}=0.1 mm and other aberrations set to zero, from the second-pass process (all/nm). Averages and standard deviations are given for a 10 frame series from −1000 to −1900 nm defocus.

	ΔC_{10}	C_{12}	C_{23}	C_{21}	C_{30}
Average	0.3	1.2	4.7	16.6	98220
Deviation	2.1	1.1	20.8	32.9	3424
True	0	0	0	0	100000

Table 3 shows a repeat of the measurement from the simulated Ronchigrams reported in Table 1, using this iterative method, which demonstrates a useful improvement in the accuracy and a reduction in the standard deviation. As an example, the measured C_{30}, which should be 100 μm, has improved from 90 ± 11 to 98 ± 3 μm. The convergence indicates that the measurement was likely successful and using more patches or more iterations has the potential to reduce the error further. More importantly, we have found this improvement to be particularly useful for the experimental measurement of higher-order aberrations.

Figs. 4–6 show experimental Ronchigrams acquired on the JEOL 2200MCO at Oxford together with simulations. In each figure (a) shows the experimental Ronchigram and (b) shows the simulated Ronchigram calculated using the aberration coefficients measured using the second-pass method as described. In Fig. 4 the aberrations were optimized, in Fig. 5 astigmatism (C_{12} or A_1) was deliberately introduced and in Fig. 6 coma (C_{21} or B_2) was deliberately introduced. The measured values are given in Table 4 in the Appendix. It is difficult to quantitatively determine how accurately the aberrations are measured, since the true values are unknown, but we have found that the negative C_5 of about a millimeter and a similar magnitude for the five-fold astigmatism (C_{56} or A_5) are compatible with values normally reported by the CEOS software on this instrument under these conditions. Additionally, the

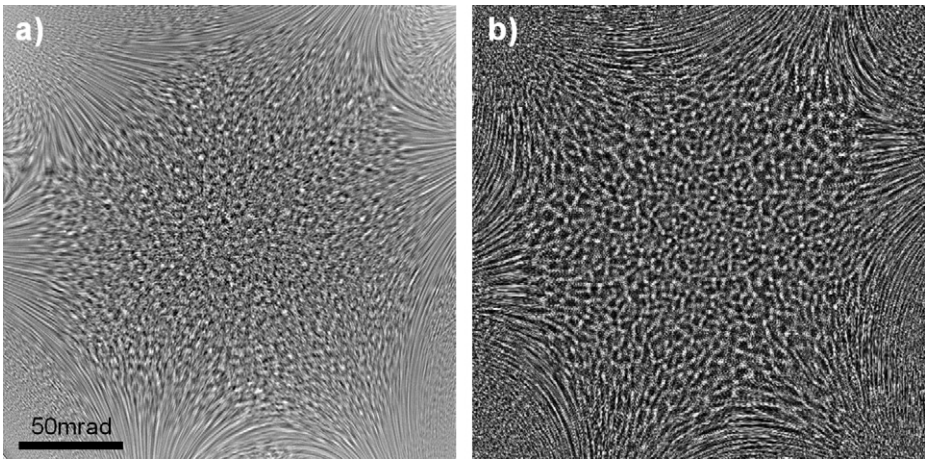

Fig. 4. (a) Experimental electron Ronchigram recorded after optimization of aberrations. (b) Simulated Ronchigram using the calculated aberration values (Column I in Table 4 in the Appendix).

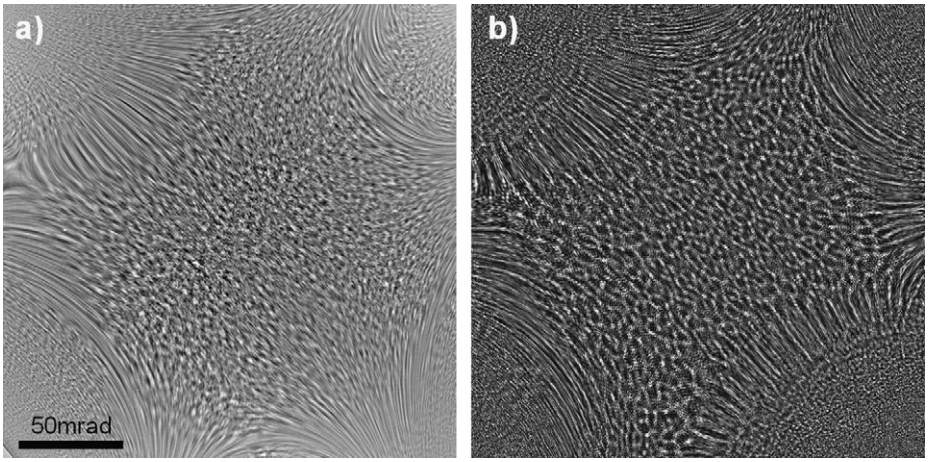

Fig. 5. (a) Experimental electron Ronchigram recorded after the introduction of two-fold astigmatism. (b) Simulated Ronchigram using the calculated aberration values (Column II in Table 4 in the Appendix).

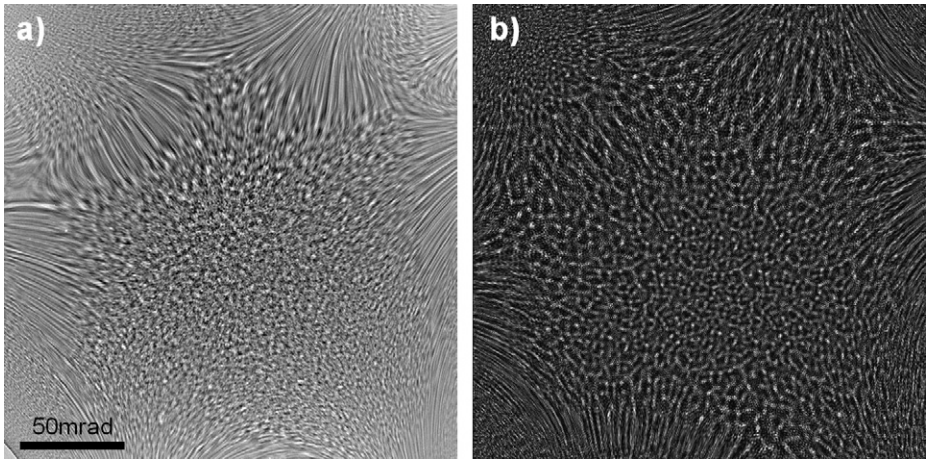

Fig. 6. (a) Experimental electron Ronchigram recorded after the introduction of coma. (b) Simulated Ronchigram using the calculated aberration values (Column III in Table 4 in the Appendix).

experimental Ronchigrams depend heavily on the fifth-order aberrations and since the overall match is reasonably good, this indicates that the measured aberrations are physically realistic. The remaining imperfections in the match are probably due to effects such as post-sample distortions, chromatic aberration, and aberrations higher than fifth-order that we have not fully accounted for, as well as errors in the simple fitting routine.

5. Conclusions

We have derived an approximation to the CTF of a Ronchigram applicable to the analysis of small sub-regions. This provides the basis for the measurement of aberrations to arbitrary order from a single Ronchigram, which should be less sensitive to drift than methods that use multiple frames. In principle, the low-order measurement component could be implemented in 'real time' since the total number of operations required for a single first order measurement (defocus and two-fold astigmatism) is little more than a single Fast Fourier Transform. A particular advantage of this method is that it provides an absolute measure of the aberrations. For comparison, the method described in [14] requires an independently calibrated defocus value to determine several constants and both the CEOS STEM tuning method and the method described in [15] (for an unknown crystal) also require a calibrated focus change. Thus an approach that provides an absolute focus value, even for an otherwise uncalibrated objective lens, offers significant benefits and is a useful complement to these previously reported methods. Post-sample aberrations due to the imaging lenses can lead to errors in the method described, but conversely this has the potential benefit of allowing the simultaneous independent measurement of both pre- and post-field aberrations, although multiple Ronchigrams would be required. For on-axis patches we have shown that the contrast transfer damping is dominated by the source size, but that away from the optic axis the chromatic aberration becomes significant. This result implies that fitting the damping envelopes at a suitable defocus should also be able to provide a measurement of both the source size and chromatic focus spread from a single Ronchigram.

Acknowledgements

A.R. Lupini and S.J. Pennycook would like to acknowledge support from the Division of Materials Science and Engineering of the U.S. Department of Energy. P. Wang, A.I. Kirkland and P.D. Nellist would like to acknowledge financial support from the Leverhulme Trust (F/08 749/B), the EPSRC (EP/F048009/1), and the Department of Materials at the University of Oxford.

Appendix A. Supplementary material

Supplementary data associated with this article can be found in the online version at doi:10.1016/j.ultramic.2010.04.006.

References

[1] P.D. Nellist, et al., Science 305 (2004) 1741.
[2] P.E. Batson, N. Dellby, O.L. Krivanek, Nature 418 (2002) 617.
[3] C. Kisielowski, et al., Microscopy and Microanalysis 14 (2008) 469.
[4] H. Sawada et al., Journal of Electron Microscopy (Tokyo), dfp030, 2009.
[5] M.H. Gass, et al., Nature Nanotechnology 3 (2008) 676.
[6] A.F. de Jong, A.J. Koster, Scanning Microscopy 6 (Suppl.) (1992) 95.
[7] M. Haider, et al., Journal of Electron Microscopy 47 (1998) 395.
[8] O.L. Krivanek, N. Dellby, A.R. Lupini, Ultramicroscopy 78 (1999) 1.
[9] R.R. Meyer, A.I. Kirkland, W.O. Saxton, Ultramicroscopy 92 (2002) 89.
[10] R.R. Meyer, A.I. Kirkland, W.O. Saxton, Ultramicroscopy 2004 (2004) 115.
[11] W.O. Saxton, Ultramicroscopy 81 (2000) 41.
[12] F. Zemlin, et al., Ultramicroscopy 3 (1978) 49.
[13] Q.M. Ramasse, A.L. Bleloch, Ultramicroscopy 106 (2005) 37.
[14] H. Sawada, et al., Ultramicroscopy 108 (2008) 1467.
[15] A.R. Lupini, S.J. Pennycook, Journal of Electron Microscopy (Tokyo) 57 (2008) 195.
[16] D. Gabor, Nature 161 (1948) 777.
[17] V. Ronchi, Applied Optics **3** (1964) 437.
[18] J.M. Cowley, Ultramicroscopy 4 (1979) 435.
[19] J.M. Rodenburg, R.H.T. Bates, Philosophical Transactions: Physical Sciences and Engineering 339 (1992) 521.
[20] J.A. Lin, J.M. Cowley, Ultramicroscopy 19 (1986) 179.
[21] O.L. Krivanek, G.Y. Fan, Scanning Microscopy 6 (Suppl.) (1992) 105.
[22] J.M. Cowley, Appl. Phys. Lett. 15 (1969) 58.
[23] E. Zeitler, M.G.R. Thomson, Optik 31 (1970) 258.
[24] K. Ishizuka, Ultramicroscopy 5 (1980) 55.
[25] J. Zhu, P.L. M, J.M. Cowley, Journal of Electron Microscopy Technique 7 (1987) 177.
[26] P.D. Nellist, J.M. Rodenburg, Ultramicroscopy 54 (1994) 61.
[27] C. Dwyer, R. Erni, J. Etheridge, Applied Physics Letters 93 (2008) 021115.
[28] R.H. Wade, J. Frank, Optik 49 (1977) 81.
[29] J. Frank, Optik 38 (1973) 519.
[30] J. Bartel, A. Thust, Physical Review Letters 101 (2008) 200801.
[31] W.O. Saxton, in: Computer Techniques for Image Processing in Electron Microscopy, Academic Press, New York, 1978.
[32] Numerical Recipes in C the Art of Scientific Computing, Cambridge University Press, 1988.